Interpreting electron-momentum distributions and nonadiabaticity in strong-field ionization

C. Hofmann,[1,*] A. S. Landsman,[1] A. Zielinski,[2] C. Cirelli,[1] T. Zimmermann,[1] A. Scrinzi,[2] and U. Keller[1]
[1]*Physics Department, ETH Zurich, CH-8093 Zurich, Switzerland*
[2]*Ludwig Maximilians Universität, Theresienstrasse 37, 80333 Munich, Germany*
(Received 14 April 2014; revised manuscript received 8 August 2014; published 8 October 2014)

We investigate whether nonadiabatic effects, rather than an initial longitudinal momentum spread, can explain the additional final momentum spread measured in strong-field ionization experiments with ultrafast laser pulses. We find that, when used consistently, a well-known nonadiabatic theory which includes an initial velocity offset yields results similar to adiabatic theory. By "consistent use" we mean that nonadiabatic theory is used also for field strength calibration of the experiment. The additional momentum spread can be accounted for by including an initial longitudinal momentum spread, as was done previously in the adiabatic case. Interestingly, when the experimental intensity is calibrated using a common *in situ* calibration method based on adiabatic assumptions, the nonadiabatic theory improves upon the adiabatic theory. This result highlights the uncertainty associated with using theory-based calibration methods, which are the most common way of calibrating experimental data in attosecond science.

DOI: 10.1103/PhysRevA.90.043406 PACS number(s): 33.20.Xx, 31.15.xg, 32.80.Rm, 33.60.+q

I. INTRODUCTION

In attosecond science, many methods and techniques rely on tunnel ionization in strong laser fields to access information about the atomic or molecular systems, such as valence electron dynamics [1]. In order to interpret the data, strong-field ionization models [2–7], building on the seminal work of Keldysh [8], are frequently used [9,10].

Electrons which are freed from their atom by a strong, elliptically polarized laser field through tunnel ionization acquire a momentum in the direction of the electric field (also referred to as the longitudinal direction) at the instance of ionization during propagation in that same field. The value of the acquired momentum depends on the phase of the field at the moment when the electron exits the tunnel and enters the continuum. This results in a final longitudinal momentum spread which can be measured at a detector. While the expressions for the initial transverse spread at the tunnel exit are well accepted, the initial longitudinal spread has long remained a matter of debate, with the usual assumption that it is equal to zero [11].

However, a recent experiment [12–14] measured final longitudinal spread that is wider than the commonly used theoretical prediction [3,15]: a result consistent with the existence of a significant longitudinal momentum spread at the tunnel exit. Subsequent work [16] showed that the double peak structure found in Ref. [12] for ellipticity $\epsilon \leqslant 0.3$ can be reproduced without the initial longitudinal spread. Based on *qualitative* observations, Li *et al.* and Sun *et al.* [16,17] concluded that the measurements in Ref. [12] were compatible with zero initial spread. However, other work [13] showed that the double peak structure observed in Ref. [12] was an artifact of radial integration, which fails at low ellipticities of laser light. Introducing a different method of elliptical integration, Hofmann *et al.* [13] analyzed again the initial longitudinal momentum spread, showing that *quantitative* agreement with the measurements in Ref. [12] is obtained if an initial longitudinal momentum spread is used, but not if that initial spread is zero.

Here, we investigate whether nonadiabatic effects, rather than an initial longitudinal spread at the tunnel exit, can account for the discrepancy between theoretical predictions in Ref. [3] and the experimental observation in Ref. [12]. In the adiabatic regime, the electron sees a quasistatic field and no photons are absorbed from the laser field. Therefore, the adiabatic limit corresponds to the pure tunneling limit. Nonadiabatic effects result in both wider momenta spreads (see Appendix C) and different initial velocity offsets at the tunnel exit. For the purposes of this investigation, we use the well-known theory developed by Perelomov, Popov, and Terent'ev [4,5] (know as PPT), which takes account of nonadiabatic effects and converges to the results obtained by Ammosov, Delone, and Krainov (ADK) [2,3] in the adiabatic limit.

We find a much better agreement with the experimental data in Ref. [12] using nonadiabatic theory, but only if we use a standard *in situ* intensity calibration introduced in Ref. [18]. However, such calibration is based on the adiabatic ADK theory [2,3], specifically on matching the final transverse momentum in elliptical polarization between theory and experiment. If we recalibrate the intensity using the nonadiabatic theory from PPT [4,5], we again find a discrepancy between theory and experimental data almost identical to that found in Ref. [12].

Our findings highlight the drawbacks of the common methods of intensity calibration widely used in attosecond science today, which are often based on some version of strong-field ionization theory. For instance, the results of Shafir *et al.* [19] were consistent with a nonadiabatic saddle point approximation: the same theory, however, which was also used to calibrate their experimental data. Similarly, Arissian *et al.* [20], showed consistency in the transverse momenta spreads with the adiabatic ADK theory [2,3], but used an adiabatic assumption of zero initial velocity to calibrate their data. In short, experimental data are calibrated with a specific theory, and later the calibrated data are used to test the exact same theory. On the other hand, current theory-independent intensity

*Corresponding author: chofmann@phys.ethz.ch

measurements are determined from laser parameters and are known to be highly imprecise [21], hence necessitating the use of theory-based calibration.

II. NONADIABATIC THEORY

Generally, adiabatic and nonadiabatic regimes are separated by the Keldysh parameter [8]

$$\gamma = \frac{\sqrt{2I_p}}{F_{\max}}\omega, \tag{1}$$

where I_p is the ionization potential of the atom (or molecule), $F_{\max}$ the maximum field amplitude, and ω the frequency of the electric field. Conditions with $\gamma \ll 1$ are adiabatic, while $\gamma \gg 1$ is considered nonadiabatic [8,11]. However, often experiments are carried out at an intermediate regime $\gamma \sim 1$; see, for example, Refs. [19,22].

The electric field of the ionizing laser pulse can be described within the dipole approximation as

$$\boldsymbol{F}(t) = \frac{F}{\sqrt{1+\epsilon^2}}\left[\cos(\omega t)\hat{\boldsymbol{x}} + \epsilon\sin(\omega t)\hat{\boldsymbol{y}}\right] f(t), \tag{2}$$

where F^2 is the peak intensity of the pulse, $F/\sqrt{1+\epsilon^2} = F_{\max}$ along the major axis, and ϵ is the ellipticity with x being the major and y the minor axis. $f(t)$ describes the envelope of the pulse with maximum $f(0) = 1$. This field, due to the absence of spatial dependence and magnetic fields which both considerably complicate the dynamics [23–25], allows for easy interpretation of classical trajectories [26,27].

To be consistent when applying a nonadiabatic theory to the final results, the laser field intensity of an experiment needs to be calibrated from nonadiabatic theory as well, which results in a smaller field strength compared to the standard adiabatic intensity calibration [18]. In Refs. [4,5], PPT derived an expression for the ionization probability depending on final electron momentum $\boldsymbol{p} = (p_x, p_y, p_z)$, based on the strong-field approximation first described by Keldysh [8]. In contrast to purely adiabatic treatments, PPT accounts for the time dependence of the field during the tunneling process. The Gaussian expansion to exponential accuracy of the ionization probability is given by [5]

$$P^{\mathrm{NA}}(\gamma,\boldsymbol{p}) \propto \exp\left\{-\frac{2I_p}{\omega}f(\gamma,\epsilon)\right\} \times \exp\left\{-\frac{1}{\omega}\left[c_x p_x^2 + c_y\left(p_y \pm p_y^{\mathrm{NA}}\right)^2 + c_z p_z^2\right]\right\}, \tag{3}$$

with

$$f(\gamma,\epsilon) := \left(1+\frac{1+\epsilon^2}{2\gamma^2}\right)\operatorname{arsinh}\left(\sqrt{\frac{\gamma^2+s_0^2}{1-s_0^2}}\right) - \frac{1+\epsilon^2-2\epsilon s_0}{2\gamma^2\left(1-s_0^2\right)}\sqrt{(1+\gamma^2)\left(s_0^2+\gamma^2\right)},$$

$$c_x := \frac{s_0(1-\epsilon^2)}{(\epsilon-s_0)(1-\epsilon s_0)}\sqrt{\frac{s_0^2+\gamma^2}{1+\gamma^2}},$$

$$c_y := \frac{\epsilon}{\epsilon-s_0}\sqrt{\frac{s_0^2+\gamma^2}{1+\gamma^2}} + \frac{s_0^2}{1-\epsilon s_0}\sqrt{\frac{1+\gamma^2}{s_0^2+\gamma^2}},$$

$$c_z := \frac{\epsilon}{\epsilon-s_0}\sqrt{\frac{s_0^2+\gamma^2}{1+\gamma^2}}.$$

The parameter $s_0 \in (0,\epsilon)$ is the solution to the transcendental equation

$$\operatorname{artanh}\left(\sqrt{\frac{s^2+\gamma^2}{1+\gamma^2}}\right) = \frac{\epsilon}{\epsilon-1}\sqrt{\frac{s^2+\gamma^2}{1+\gamma^2}}, \tag{4}$$

and p_y^{NA} is the most probable p_y final momentum offset along the minor axis of polarization

$$p_y^{\mathrm{NA}} = \frac{F_{\max}}{\omega}(\epsilon-s_0)\sqrt{\frac{1+\gamma^2}{1-s_0^2}}. \tag{5}$$

Throughout the paper superscript NA is used to indicate nonadiabatic theory, and A is used to indicate adiabatic theory.

In the expansion (3), terms of higher order than $[\boldsymbol{p}^2 \pm (\boldsymbol{p}_y^{\mathbf{NA}})^2]$ were neglected. When $|\epsilon| \to 1$, however, c_x goes to zero and higher-order terms play an important role [5]. Thus, the accuracy of formula (3) decreases as the laser field approaches circular polarization.

In the adiabatic limit $\gamma \ll 1$, the probability factor of (3) described by $f(\gamma,\epsilon)$ simplifies to

$$P^{\mathrm{A}} \propto \exp\left\{-\frac{2(2I_p)^{2/3}}{3F_{\max}}\right\}, \tag{6}$$

which is the well-known exponential dependence derived by Keldysh [8].

III. SEMICLASSICAL SIMULATION

Classical trajectory Monte Carlo (CTMC) simulations of the electron trajectories after tunnel ionization were calculated for both adiabatic and nonadiabatic tunneling theory. Clouds of 300 000 electrons simulated the ionized part of the wave function. For ellipticities <0.2, many electrons rescatter close to the parent ion [28], and quantum mechanical effects are expected to become important. Since these cannot be described in a classical framework, simulations were only performed for $\epsilon \geqslant 0.2$, and trajectories coming closer than 5 a.u. were discarded.

A. Adiabatic CTMC

For the adiabatic CTMC, the TIPIS model (tunnel ionization in parabolic coordinates with induced dipole and Stark shift) [29–31] was used to find the exit points (see also Appendix D). All the initial conditions for the adiabatic case as well as the analysis for best-fitting initial longitudinal momentum spread are described in detail in Ref. [13].

B. Nonadiabatic CTMC

For the nonadiabatic CTMC, ensembles of electrons were generated with momentum distributions and probabilities

based on the semiclassical analysis of the PPT theory. The original semiclassical analysis [5] is centered around a single trajectory emerging from the tunnel exit with zero initial longitudinal momentum at the instant when $F(t) = F_{\max}$. In order to account for trajectories emerging at different times, we introduce the time dependence simply by letting γ (and consequently s_0) depend on the actual value of the field $F(t)$. The initial transverse momenta were centered around the most probable transverse initial momentum given by [5]

$$p^{\mathrm{NA}}_{\mathrm{initial}}(t) = p^{\mathrm{NA}}_{y}(t) - \frac{\epsilon F_{\max}}{\omega}, \qquad \sigma^{\mathrm{NA}}_{\perp,y/z}(t) = \sqrt{\frac{\omega}{2c_{y/z}(t)}}, \tag{7}$$

with standard deviations $\sigma^{\mathrm{NA}}_{\perp,y/z}$ in-plane and out-of-plane of polarization, respectively. The position of the tunnel exit changes with time as [5]

$$\boldsymbol{r}^{\mathrm{NA}}(t) = \frac{\boldsymbol{F}(t)}{\omega^2}\left(\sqrt{\frac{1+\gamma^2(t)}{1-s_0^2(t)}} - 1\right). \tag{8}$$

Other nonadiabatic theories exist which provide initial conditions at the tunnel exit [7,32], but they are limited to the special case of linear (and circular) polarization.

C. Time integration

All adiabatic and nonadiabatic ensembles were propagated by numerically integrating the classical Newton's equation of motion

$$\ddot{\boldsymbol{r}}(t) = -\boldsymbol{F}(t) - \nabla\left[\frac{-1}{\sqrt{r^2(t)+\mathrm{SC}}} - \alpha_{\mathrm{I}}\frac{\boldsymbol{F}(t)\cdot\boldsymbol{r}(t)}{r^3(t)}\right], \tag{9}$$

where the first term in the gradient is the Coulomb force from the parent ion with the soft-core constant SC and the second term is the induced dipole of the ion with polarizability α_I due to the laser field.

Some more details on differences and agreements between the applied theories and models can be found in Appendix A.

IV. EXPERIMENT

Details on the experiment can be found in Refs. [12,13]. Helium atoms from a cold gas jet were ionized by a strong laser pulse with approximately 0.7–0.8 PW/cm^2 peak intensity at a central wavelength of 788 nm, 33 fs pulse duration FWHM, and varying ellipticity; the carrier-envelope offset phase was not stabilized [33]. In a COLTRIMS (cold target recoil ion momentum spectrometer) [34] setup, the final momenta of electrons, once the laser pulse had passed, were recorded (Fig. 1). In the time-of-flight direction, the momentum resolution of the detector was 0.1 a.u. In the gas jet direction, thermal spread led to a resolution estimate of $\leqslant$0.9 a.u.

A. Time-dependent Schrödinger equation

To ensure that the additional longitudinal momentum spread measured in the experiment (Fig. 2) reflected underlying physics and was not the result of unknown experimental

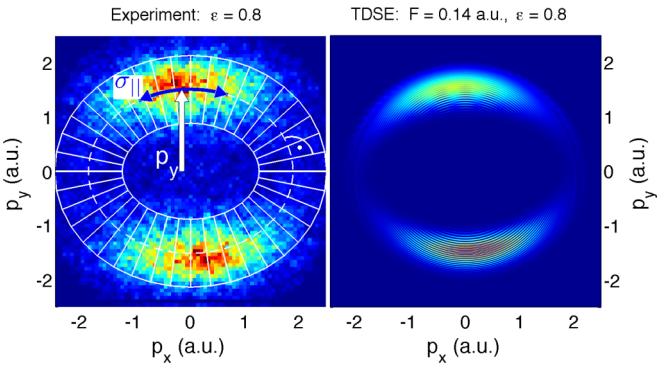

FIG. 1. (Color online) 2D momentum spread. The final electron-momentum distributions in the plane of polarization as measured in COLTRIMS and calculated by TDSE shows two distinct maxima separated by $2p_y$ along the minor axis. In TDSE, wave packets from different cycles of the pulse interfere. In the experimental data, orthogonal segments for elliptical integration are indicated [13].

noise, we analyzed time-dependent Schrödinger simulations (TDSE, Fig. 1). The computations were performed for a single-electron model with screened potential

$$V(r) = \frac{-1-\exp\{-\alpha r\}}{r}, \tag{10}$$

where $\alpha = 2.1325$ was adjusted to reproduce the lowest few helium bound-state energies, and field strength $F^{\mathrm{NA}} = 0.14$ au. The nonadiabatically calibrated field strength F^{NA} was chosen instead of the adiabatically calibrated $F^{\mathrm{A}} = 0.151$ a.u., based on the fact that it leads to better agreement with experimental momentum spreads. Photoelectron spectra were calculated by the time-dependent surface flux (t-SURFF) technique [35] and momentum spectra were converged to ensure errors of $\lesssim$1% for the momentum spread.

B. Experimental results

With this procedure, we found an additional longitudinal spread from TDSE simulations as compared to theoretical predictions, in agreement with experimental results in Ref. [12]. In particular, any intensity computed had ratios of $\sigma^{\mathrm{TDSE}}_{||}/\sigma^{\mathrm{NA}}_{||} > 1$, where $\sigma^{\mathrm{TDSE}}_{||}$ and $\sigma^{\mathrm{NA}}_{||}$ are the longitudinal spreads extracted from the TDSE simulations and predicted by the nonadiabatic theory (11), respectively. The momentum spreads found in TDSE agree with experimental measurements at high ellipticity and exceed the measured values at lower ellipticity (see Fig. 2). The deviations could be due to the difference in the assumptions used in the implementation of TDSE [35] and the actual experimental conditions [12]. To summarize, the TDSE results further confirm that the measured additional longitudinal spread reflects underlying physics of tunnel ionization that cannot be accounted for within the current theoretical framework.

V. LONGITUDINAL SPREAD COMPARED

All the simulation results and the experimental data were analyzed with the identical method, described in Ref. [13]. In particular, the longitudinal spread and the angular momentum distribution were extracted using elliptical integration.

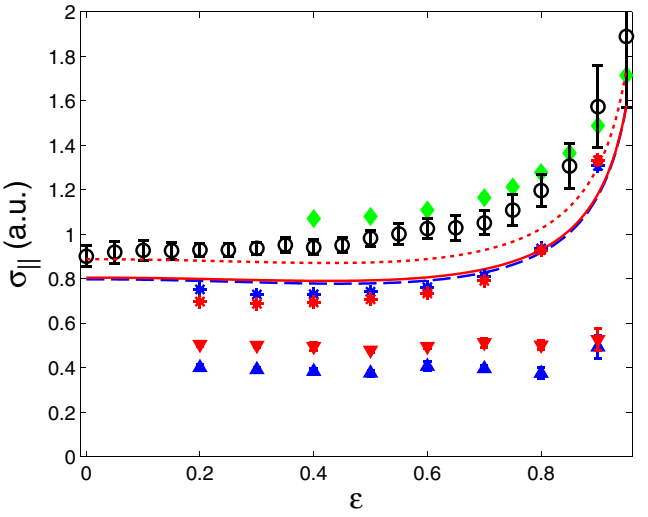

	type	theory	field strength	Ref.
○	experiment			[12]
– –	analytical	ADK, A	$F^{\mathrm{A}} = 0.151$ a.u.	(12)
···	analytical	PPT, NA	F^{A}	(11)
—	analytical	PPT, NA	$F^{\mathrm{NA}} = 0.14$ a.u.	(11)
∗	CTMC	ADK, A	F^{A}	(6)
▲	$\sigma_{\parallel}^{\mathrm{in}}$	ADK, A	F^{A}	(6)
∗	CTMC	PPT, NA	F^{NA}	(3)
▼	$\sigma_{\parallel}^{\mathrm{in}}$	PPT, NA	F^{NA}	(3)
◆	TDSE		F^{NA}	[35]

FIG. 2. (Color) Longitudinal momentum spread. The best-fitting initial longitudinal momenta spreads for the adiabatic and nonadiabatic theories are shown as blue and red triangles, respectively. These spreads were obtained by requiring the best fit between CTMC simulations and experimental data. All error bars show the 98% confidence interval of the corresponding fitting process to extract the respective value. A = adiabatic, NA = nonadiabatic.

A. Nonadiabatic theoretical predictions

Analytically, nonadiabatic theory [5] gives rise to a wider final longitudinal momentum spread,

$$\sigma_{\parallel}^{\mathrm{NA}} = \sqrt{\frac{\omega}{2c_x}}, \tag{11}$$

than adiabatic theory [15] valid for any ellipticity $|\epsilon| < 1$,

$$\sigma_{\parallel}^{\mathrm{A}} = \sqrt{\frac{3\omega}{2\gamma^3(1-\epsilon^2)}} \leqslant \sigma_{\parallel}^{\mathrm{NA}}, \tag{12}$$

for the same peak field strength. In Fig. 2, the analytical formula (11) for the nonadiabatic final longitudinal momentum spread (red dashed line) calculated at $F^{\mathrm{A}} = 0.151$ a.u. (adiabatic field calibration) almost agrees with the experimental data [12] within error bars (black circles). It is certainly always wider than the adiabatic formula (12) calculated at the same field strength (blue solid line). At first glance, one may conclude from this that an initial longitudinal momentum spread is not necessary to explain the experimental data in Ref. [12], once nonadiabatic effects are taken into account.

B. Nonadiabatic intensity calibration of experiments

However, to be fully consistent in the applied model, the intensity of the laser pulse in the experiment also must be calibrated [18] using the same nonadiabatic theory (5), which leads to a larger p_y^{NA} offset than adiabatic theory [36], where the adiabatic momentum offset is given by [19]

$$p_y^{\mathrm{A}} = \frac{\epsilon F_{\max}}{\omega}. \tag{13}$$

This difference is due to the initial transverse momentum offset (7). Consequently, the field strength constant used in the CTMC for the completely nonadiabatic model was only $F^{\mathrm{NA}} = 0.14$ a.u. compared to $F^{\mathrm{A}} = 0.151$ a.u. in the adiabatic case (see Fig. 4). As a consequence of the nonadiabatic field strength calibration, the final longitudinal momentum spread curve given by Eq. (11) is shifted down to the solid red line in Fig. 2, where it agrees almost exactly with the analytical formula (12) for the adiabatic case (solid blue).

C. CTMC results

The CTMC results show a similar pattern: with zero initial longitudinal momentum spread, the adiabatic (blue ∗) and nonadiabatic (red ∗) CTMC again almost agree. Consequently, comparable initial longitudinal momentum spreads are necessary to reproduce the experimental momentum distribution.

As an example, Fig. 3 compares the angular momentum distribution extracted by elliptical integration between nonadiabatic CTMC and experimental data for ellipticity $\epsilon = 0.4$ and for 0 or 0.5 a.u. initial longitudinal momentum spread. For every ellipticity and initial longitudinal momentum spread pair, the mean square error between the experimental and the simulation angular distribution is calculated. The best-fitting initial spread with minimal error is then found by interpolation. More details on the fitting process between the CTMC and experimental data can be found in Ref. [13]. The resulting initial longitudinal momentum spreads are shown in Fig. 2 as blue ▲ for the adiabatic and red ▼ for the nonadiabatic case.

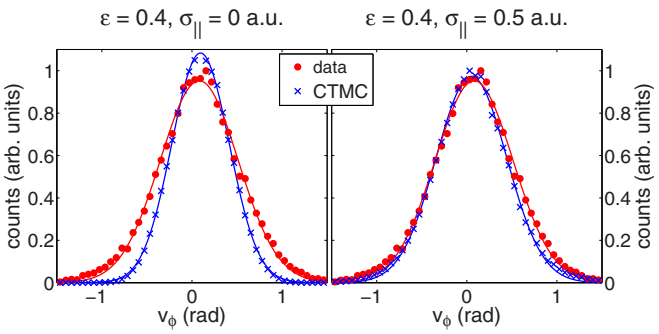

FIG. 3. (Color online) Angular momentum distribution. The red dots in both panels show the top half of the momentum distribution (bottom is symmetric). Blue ×'s in the left panel are the final distribution when starting the nonadiabatic CTMC with zero, and on the right with 0.5 a.u. initial longitudinal momentum spread. Solid lines represent Gaussian fits. ϕ is counted anticlockwise from the y axis.

Comparing the CTMC with analytical calculations, the CTMC final spreads are a bit smaller than the analytical formula (except for when $\epsilon \to 1$, when the accuracy of the expansion to second order breaks down). For the adiabatic CTMC, this is due to the field strength averaging effect of electrons which are ionized in optical cycles not located at the center of the pulse and therefore have a lower (local) maximum field strength [13]. For the nonadiabatic CTMC, field strength averaging effects and the time dependence introduced in Eq. (3) reduce the final CTMC spread compared to the analytic curve.

In summary, it follows that nonadiabatic effects alone cannot explain the additional longitudinal momentum spread observed at the detector in the experiment, if the intensity is recalibrated using the same nonadiabatic theory.

VI. INTENSITY CALIBRATION

As demonstrated above, the results of adiabatic and nonadiabatic theory are very similar, and so is the initial longitudinal momentum spread needed to quantitatively match the experiment. This raises another important issue. Usually, the laser peak intensity is determined from the momentum offset of the electrons along the minor axis, because it is the most accurate method available [18]. However, this method depends strongly on the applied theory to calculate the mapping between offset and intensity.

For elliptical polarization, nonadiabatic theories predict an initial transverse momentum offset (7) [5]. As a consequence, the most probable final transverse momentum in the nonadiabatic description is larger than that in the adiabatic limit,

$$p_{\perp,\mathrm{f}}^{\mathrm{NA}} > p_{\perp,\mathrm{f}}^{\mathrm{A}} = \frac{\epsilon F_{\max}}{\omega}, \tag{14}$$

for identical field parameters. The measured $p_\perp$ of the experiment is compared to theoretical formulas (neglecting the influence of the ion Coulomb force), results of single classical trajectory simulations, or CTMC simulations.

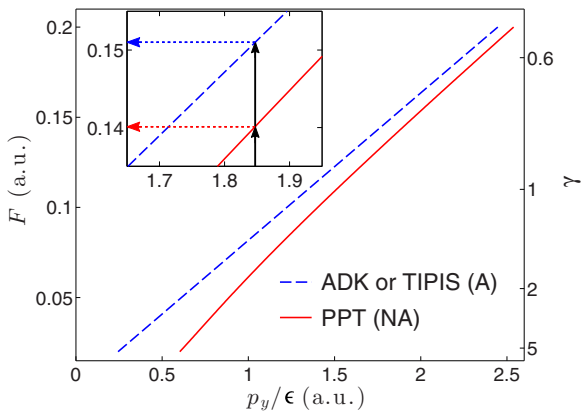

FIG. 4. (Color online) Intensity calibration. The blue dashed line shows the adiabatic momentum offset p_y^{A} (13); the red solid line is p_y^{NA} as calculated by single trajectory simulation and corresponds to Eq. (5). Inset: The experimentally measured $p_y/\epsilon = 1.85$ a.u. (black solid arrows, see Fig. 1) yields $F^{\mathrm{A}} = 0.151$ a.u. and $F^{\mathrm{NA}} = 0.14$ a.u. The larger the Keldysh parameter γ, the more pronounced is the nonadiabatic effect.

In this experiment, the Keldysh parameter varies between 0.51 and 0.73 [12], which is in a very high intensity regime. With increasing γ (in practice, this is usually achieved by decreasing the field strength), the difference between adiabatic and nonadiabatic intensity calibration grows substantially (see Fig. 4). With a measured $p_y^{\mathrm{exp}}/\epsilon$ of 0.75 a.u. for example, the nonadiabatic calibration yields a field strength which is only 58% of the adiabatic calibration value. In laser peak intensity, the nonadiabatic value is only 34% of the adiabatic calibration for this example, due to the square. On the other hand, to the best of our knowledge, there is no alternative method to determine the laser intensity at an intrinsic accuracy of $\leqslant$20% [18].

VII. CONCLUSION

In conclusion, we have shown that consistent application of either adiabatic or nonadiabatic theory cannot explain fully the longitudinal momentum spread that was measured in Ref. [12]. When used with CTMC calculations, the agreement of both theories with the experiment may be achieved by including an initial longitudinal momentum spread, pointing to a need for further theoretical developments. Moreover, further investigation is required to establish better than the current state of the art calibration methods for the $\gamma \sim 1$ regime, where a majority of experiments in attosecond science take place.

ACKNOWLEDGMENTS

This research was supported by the NCCR MUST, funded by the Swiss National Science Foundation (SNSF), by ETH Research Grant No. ETH-03 09-2, by an SNSF equipment grant, and by an SNSF project grant. Our ultrafast activities are supported by the ETH Femtosecond and Attosecond Science and Technology (ETH-FAST) initiative as part of the NCCR MUST program. A.Z. acknowledges support by the Austrian Science Fund (FWF) and by the Munich Center for Advanced Photonics.

APPENDIX A: APPROXIMATIONS IN THEORIES

Table I shows an overview of the theories which are discussed in this work, comparing their characteristics, and lists relevant references.

Some approximations in analytical models describing strong-field ionization are commonly used. Most notably, the so-called strong-field approximation (SFA). In SFA, it is assumed that the Coulomb potential of the parent ion can be neglected once an electron has entered the continuum [11], also known as short-range potential. Thus, the dynamics of an electron wave packet after ionization is completely determined by the strong laser field. Conversely, the laser field is usually neglected when considering a bound wave function as the initial state before the ionization. Table II collects the different approximations and model assumptions in the presented theories.

TABLE I. Overview over characteristics of theories.

Name	Type	r_{exit}	Field dependence	v_{initial}	$\sigma_\perp$	$\sigma_{\parallel,\text{final}}$	Ref.
Keldysh or ADK	Adiab.	I_p/F	$\propto \exp\{-\frac{2(2I_p)^{3/2}}{3F}\}$	0	$\sqrt{\frac{\omega}{2\gamma}}$	$\sqrt{\frac{3\omega}{2\gamma^3(1-\epsilon^2)}}$	[2,8,11]
Parabolic	Adiab.	$\frac{I_p+\sqrt{I_p^2-4\beta_2 F}}{2F}$	$\propto \exp\{-\frac{2(2I_p)^{3/2}}{3F}\}$	0	$\sqrt{\frac{\omega}{2\gamma}}$	$\sqrt{\frac{3\omega}{2\gamma^3(1-\epsilon^2)}}$	[29–31]
PPT	Nonadiab.	$\leqslant I_p/F$	$>$	$v_{\perp,i} \neq 0$	$>$	$>$	[4,5]

Contrary to analytical methods, CTMC simulations only use these model assumptions to determine the initial conditions (exit point, initial velocity, ionization time distribution), but then do take account of the Coulomb force of the parent ion during the propagation of ionized electrons. An example of that is the TIPIS model [29–31], which uses parabolic coordinates and Stark-shifted ionization potential to solve the quasistatic Schrödinger's equation for the exit point and includes both the ion Coulomb force and the induced dipole during the propagation of the electron.

APPENDIX B: FIELD DEPENDENCE

In the adiabatic limit of strong-field ionization, the dynamics of the laser field are so slow compared to the typical dynamics of a bound electron that the field can be approximated as quasistatic. Thus, the electron does not absorb any photons and is purely tunnel ionizing. In this $\gamma << 1$ limit of the Keldysh parameter

$$\gamma = \omega \frac{\sqrt{2I_p}}{F},$$

the ionization probabilty goes with the Keldysh exponent for the instantaneous field strength dependence (to exponential accuracy) [8,11]

$$P^{\text{A}}(F) \propto \exp\left\{-\frac{2(2I_p)^{3/2}}{3F}\right\} = \exp\{-\Phi^{\text{A}}\},$$
$$\Phi^{\text{A}}(\gamma) := \frac{2(2I_p)^{3/2}}{3}\frac{\gamma}{\omega\sqrt{2I_p}}, \tag{B1}$$

and is independent of the field frequency.

On the other hand, pure single-photon ionization in high-frequency fields scales linearly with the field intensity. Nonadiabatic theories for strong-field ionization occupy a range between these two limits, where an electron wave packet does feel the dynamics of the field and also absorbs some photons, but it is still tunneling out of the potential ($\gamma \gtrsim 1$). Consequently, the field strength dependence in nonadiabatic theories is a bit less steep than that in the adiabatic case. In the formulation by PPT [4,5], it is

$$P^{\text{NA}}(\gamma) \propto \exp\left\{-\frac{2I_p}{\omega} f(\gamma,\epsilon)\right\} = \exp\{-\Phi^{\text{NA}}\},$$
$$\Phi^{\text{NA}}(\gamma) := \frac{2I_p}{\omega} f(\gamma,\epsilon), \tag{B2}$$

where $f(\gamma,\epsilon)$ introduces the field strength (and frequency) dependence. Figure 5 compares the field dependence through the Keldysh parameter for a fixed $\omega = 0.06$ (wavelength 788 nm) and I_p of helium.

It illustrates $\Phi^{\text{NA}} \leqslant \Phi^{\text{A}}$, meaning that the ionization probability in the nonadiabatic description decreases more slowly with decreasing field strength than in the adiabatic approximation.

TABLE II. Overview over assumptions.

Name	A or NA	r_{exit}
Keldysh or ADK	Quasistatic	Triangular barrier
Parabolic	Quasistatic	Coulomb+field
PPT	Time dependent	Triangular barrier

APPENDIX C: MOMENTUM SPREAD

This fact, in turn, leads also to wider momentum spread predictions in the nonadiabatic theory. The longitudinal final momentum spread $\sigma_{\parallel}$ (parallel to the laser field at the tunnel exit) for example is due to electrons being ionized at different phases of the field and therefore gaining different longitudinal momentum during the propagation in the remainder of the pulse. For the transverse momentum spread $\sigma_\perp$ (orthogonal to the laser field at the tunnel exit), the argument is similar. In Ref. [11], it is shown nicely that the transverse spread can be

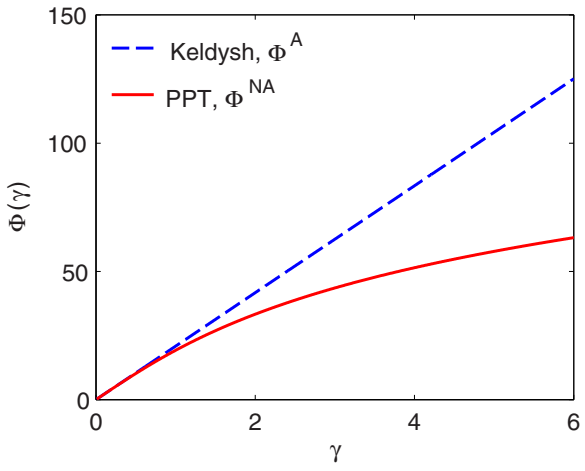

FIG. 5. (Color online) Field dependence of the ionization probability, depending on the Keldysh parameter γ, compared for an adiabatic (blue dashed line) and a nonadiabatic (red solid line) model. Smaller $\Phi(\gamma)$ means higher ionization probability.

derived by considering a modified Keldysh parameter,

$$\tilde{\gamma} := \omega \frac{\sqrt{2I_\mathrm{p} + p_\perp^2}}{F}, \tag{C1}$$

depending on the transverse momentum $p_\perp$ in Eq. (B1).

APPENDIX D: EXIT RADIUS

In the pure quasistatic, adiabatic limit, applying the field direction model [11], the exit radius is simply the point where the electron can exit the potential barrier (approximated as a triangle) with the ground-state energy $-I_\mathrm{p}$, which results in

$$r_\mathrm{exit}^\mathrm{A} = \frac{I_\mathrm{p}}{F}. \tag{D1}$$

In parabolic coordinates, the Schrödinger equation for the quasistatic problem can be solved exactly, yielding a third-order equation for the exit point which can be approximated to second order [13]:

$$r_\mathrm{exit,parab}^\mathrm{A} = \frac{I_\mathrm{p} + \sqrt{I_\mathrm{p}^2 - 4\beta_2 F}}{2F}, \qquad \beta_2 = 1 - \frac{\sqrt{2I_\mathrm{p}}}{2}. \tag{D2}$$

Since tunneling electrons in the nonadiabatic picture can absorb some photons, they gain energy and exit the potential barrier a bit earlier than in the adiabatic picture. In the formalism by PPT [5], it is given by

$$r_\mathrm{exit}^\mathrm{NA} = \frac{F}{\omega^2}\left(\sqrt{\frac{1+\gamma^2}{1-s_0^2}} - 1\right) \leqslant \frac{I_\mathrm{p}}{F}, \tag{D3}$$

where $s0 \in (0,\epsilon)$ is a parameter depending on γ.

The differences in exit radii have, however, only negligible influence on the final momentum of electrons.

[1] L. Gallmann, C. Cirelli, and U. Keller, Annu. Rev. Phys. Chem. **63**, 447 (2012).
[2] M. V. Ammosov, N. B. Delone, and V. P. Krainov, Sov. Phys. JETP **64**, 1191 (1986).
[3] N. B. Delone and V. P. Krainov, J. Opt. Soc. Am. B **8**, 1207 (1991).
[4] A. M. Perelomov, V. S. Popov, and M. V. Terent'ev, Sov. Phys. JETP **23**, 207 (1966).
[5] A. M. Perelomov, V. S. Popov, and M. V. Terent'ev, Sov. Phys. JETP **24**, 207 (1967).
[6] H. R. Reiss, Phys. Rev. A **22**, 1786 (1980).
[7] G. L. Yudin and M. Y. Ivanov, Phys. Rev. A **64**, 013409 (2001).
[8] L. V. Keldysh, Sov. Phys. JETP **20**, 1307 (1965).
[9] H. Akagi, T. Otobe, A. Staudte, A. Shiner, F. Turner, R. Dörner, D. M. Villeneuve, and P. B. Corkum, Science **325**, 1364 (2009).
[10] M. Uiberacker, T. Uphues, M. Schultze, A. J. Verhoef, V. Yakovlev, M. F. Kling, J. Rauschenberger, N. M. Kabachnik, H. Schröder, M. Lezius, K. L. Kompa, H.-G. Muller, M. J. J. Vrakking, S. Hendel, U. Kleineberg, U. Heinzmann, M. Drescher, and F. Krausz, Nature (London) **446**, 627 (2007).
[11] M. Y. Ivanov, M. Spanner, and O. Smirnova, J. Mod. Opt. **52**, 165 (2005).
[12] A. N. Pfeiffer, C. Cirelli, A. S. Landsman, M. Smolarski, D. Dimitrovski, L. B. Madsen, and U. Keller, Phys. Rev. Lett. **109**, 083002 (2012).
[13] C. Hofmann, A. S. Landsman, C. Cirelli, A. N. Pfeiffer, and U. Keller, J. Phys. B: At. Mol. Opt. Phys. **46**, 125601 (2013).
[14] A. S. Landsman, C. Hofmann, A. N. Pfeiffer, C. Cirelli, and U. Keller, Phys. Rev. Lett. **111**, 263001 (2013).
[15] V. Mur, S. Popruzhenko, and V. Popov, Sov. Phys. JETP **92**, 777 (2001).
[16] M. Li, Y. Liu, H. Liu, Q. Ning, L. Fu, J. Liu, Y. Deng, C. Wu, L. Y. Peng, and Q. Gong, Phys. Rev. Lett. **111**, 023006 (2013).
[17] X. Sun, M. Li, J. Yu, Y. Deng, Q. Gong, and Y. Liu, Phys. Rev. A **89**, 045402 (2014).
[18] A. S. Alnaser, X. M. Tong, T. Osipov, S. Voss, C. M. Maharjan, B. Shan, Z. Chang, and C. L. Cocke, Phys. Rev. A **70**, 023413 (2004).
[19] D. Shafir, H. Soifer, B. D. Bruner, M. Dagan, Y. Mairesse, S. Patchkovskii, M. Y. Ivanov, O. Smirnova, and N. Dudovich, Nature (London) **485**, 343 (2012).
[20] L. Arissian, C. Smeenk, F. Turner, C. Trallero, A. V. Sokolov, D. M. Villeneuve, A. Staudte, and P. B. Corkum, Phys. Rev. Lett. **105**, 133002 (2010).
[21] A. L'Huillier, L. A. Lompre, G. Mainfray, and C. Manus, J. Phys. B: At. Mol. Opt. Phys. **16**, 1363 (1983).
[22] P. Eckle, A. N. Pfeiffer, C. Cirelli, A. Staudte, R. Dörner, H. G. Muller, M. Büttiker, and U. Keller, Science **322**, 1525 (2008).
[23] A. S. Landsman, S. A. Cohen, and A. H. Glasser, Phys. Rev. Lett. **96**, 015002 (2006).
[24] A. S. Landsman, S. A. Cohen, and A. H. Glasser, Phys. Plasmas **11**, 947 (2004).
[25] S. A. Cohen, A. S. Landsman, and A. H. Glasser, Phys. Plasmas **14**, 072508 (2007).
[26] P. B. Corkum, Phys. Rev. Lett. **71**, 1994 (1993).
[27] K. C. Kulander, K. J. Schafer, and J. L. Krause, in *Super-Intense Laser-Atom Physics*, edited by B. Piraux, A. L'Huillier, and K. Rzewski (Springer, New York, 1993), pp. 95–110.
[28] A. S. Landsman, A. N. Pfeiffer, C. Hofmann, M. Smolarski, C. Cirelli, and U. Keller, New J. Phys. **15**, 13001 (2013).
[29] L.-B. Fu, J. Liu, J. Chen, and S.-G. Chen, Phys. Rev. A **63**, 043416 (2001).
[30] L. D. Landau and E. M. Lifshitz, *Quantum Mechanics* (Pergamon, Oxford, 1977).
[31] A. N. Pfeiffer, C. Cirelli, M. Smolarski, D. Dimitrovski, M. Abu-samha, L. B. Madsen, and U. Keller, Nat. Phys. **8**, 76 (2012).
[32] D. I. Bondar, Phys. Rev. A **78**, 015405 (2008).

[33] H. R. Telle, G. Steinmeyer, A. E. Dunlop, J. Stenger, D. H. Sutter, and U. Keller, Appl. Phys. B **69**, 327 (1999).

[34] R. Dörner, V. Mergel, O. Jagutzki, L. Spielberger, J. Ullrich, R. Moshammer, and H. Schmidt-Böcking, Phys. Rep. **330**, 95 (2000).

[35] L. Tao and A. Scrinzi, New J. Phys. **14**, 013021 (2012).

[36] R. Boge, C. Cirelli, A. S. Landsman, S. Heuser, A. Ludwig, J. Maurer, M. Weger, L. Gallmann, and U. Keller, Phys. Rev. Lett. **111**, 103003 (2013).